

Bioinspiration & Biomimetics



PAPER

Maneuvering and stabilization control of a bipedal robot with a universal-spatial robotic tail

RECEIVED
3 August 2018

REVISED
7 November 2018

ACCEPTED FOR PUBLICATION
16 November 2018

PUBLISHED
6 December 2018

William S Rone, Yujiong Liu^{ORCID} and Pinhas Ben-Tzvi¹^{ORCID}

Robotics and Mechatronics Laboratory, Department of Mechanical Engineering, Virginia Tech, Blacksburg, VA 24060, United States of America

¹ Author to whom any correspondence should be addressed.

E-mail: wsrone@vt.edu, yjliu@vt.edu and bentzvi@vt.edu

Keywords: robotic tails, biomimetics, biped robot, control

Abstract

This paper analyzes control methodologies to implement maneuvering and stabilization behaviors in a bipedal robot using a bioinspired robotic tail. Looking to nature, numerous animals augment their legs' functionality using a tail nature, numerous animals augment their legs' functionality using a tail to assist with both maneuvering and stabilization; looking to the robotics literature, previous research primarily focuses on single-mass, pendulum-like tails designed to perform a specific task. The overarching goal of this research is to study how bioinspired tail designs may be used in conjunction with low-complexity leg designs to achieve high-performance behaviors. In pursuit of this goal, this paper connects the serpentine universal-spatial robotic tail (USRT) with a biped consisting of a pair of Robotic Modular Legs to study the outer- and inner-loop control considerations necessary to achieve yaw-angle turning and stable leg lifting. The design and modeling of the tail and leg subsystems are presented, along with considerations for sensing the USRT's configuration in real-time. In addition, two inner-loop controllers that map desired tail trajectories into actuation commands are presented: a prescribed velocity approach that only utilizes motor feedback, and a prescribed torque approach that incorporates both feedforward consideration of the tail dynamics and feedback consideration from the tail sensing. Two outer-loop controllers—one for yaw-angle steering (maneuvering), and one for roll-angle disturbance rejection when lifting a foot (stabilization)—are also defined. Case studies including simulation and experimental results are used to validate the outer-loop control approaches.

1. Introduction

The dominant paradigm in biomimetic and bioinspired bipedal robot design is to mimic humanoid locomotion. However, looking to nature, an alternative approach for bipedal locomotion is one in which part of the body mass is carried in front of and behind the legs in neck and tail structures. Ostriches carry their head and articulated necks in front of their legs, with the bulk of their abdomen behind their legs [1]. Mammalian ground pangolins exhibit bipedal walking and running by balancing their head and body with a tail behind their legs [2]. Extant lizards demonstrate a dynamically stable bipedal run, with the tail helping to counterbalance the raised torso and fore legs [3]. Studies of fossil record also show a variety of functionalities provided by bipedal dinosaurs' tails, including active counter balancing

while walking/running [4] and reduced inertia for turning [5]. These bipeds, along with a variety of quadrupedal animals with tails, provide ample motivation for the consideration of robotic tails on-board legged platforms. The key benefit of a tail-like structure on-board a biped is the ability to generate loading independent of the ground contact. During a dynamically stable gait cycle, the nature of contact between the robot and ground changes with zero, one or two legs in contact at different times. A tail-like structure is capable of generating its loading at all times regardless of ground contact. Furthermore, current bipedal systems require the leg control to synthesize motor inputs based on propulsion, maneuvering and stabilization considerations. A tail-like structure could help to offset some of the maneuvering and stabilization considerations from the legs, allowing for a simpler leg controller to be used in conjunction

with a tail controller. Furthermore, this reduction in required leg functionality could also be used to enable simpler leg mechanical designs.

In terms of dynamical functionalities (maneuvering and stabilization), the pendulum tail was believed to be the most efficient and the simplest analog of the actual tail. However, recent researches [6, 7] have revealed that, even from dynamical perspectives, the biomimetic multi-link tail possesses several unique advantages including higher generated inertia loadings, volumetric center-of-mass workspaces, and the complaint-to-obstacle properties.

To explore the new paradigm, this paper analyzes inner- and outer-loop control considerations of a bioinspired robotic tail mounted to a bipedal robot, for which a design concept is shown in figure 1. The robotic tail applied the authors' prior works on the universal-spatial robotic tail (USRT) [8] and the biped consists of a pair of the RMLeg modules [9]. Outer-loop control laws are formulated to generate maneuvering and stabilizing desired tail trajectories, and inner-loop control laws map these desired trajectories into motor commands capable of executing them. Simulations of the tailed-bipedal robot are used to demonstrate these control laws, and hardware-in-the-loop (HIL) experiments using a physical tail prototype in conjunction with a legged platform simulation are used to validate the simulated loading. An overview of the case studies can be found in table 1.

The paper is organized as follows: section 2 highlights previous research into robotic tails and hyper redundant robot control. Sections 3 and 4 describe the design and modeling of the robotic tail (section 3) and biped (section 4) subsystems under consideration. Section 5 describes the tail's sensing and inner-loop controller. Sections 6 and 7 describe the implementation of the maneuvering and stabilization outer-loop control functionalities, respectively. Section 8 concludes the paper and describes planned future work.

2. Background

This section highlights prior work associated with both robotic tails (section 2.1) and controlling hyper redundant robotic structures (section 2.2).

2.1. Robotic tails

Existing research into robotic tails can be categorized by the desired functionality of the tail. Tail functionalities to aid propulsion include rapid acceleration and deceleration [10] and actuating walking in passively compliant legs [11]. Tail functionalities to aid maneuvering include midair re-orientation [12, 13] and yaw-angle turning [14, 15]. Tail functionalities to aid stabilization include disturbance rejection due to external loading [16], disturbance rejection due to leg actuation [17] and active center-of-mass adjustment during locomotion [18].

Table 1. Overview of the case studies.

Task	Simulation (ADAMS/MATLAB Co-simulation)	Experiment (ADAMS-USRT HIL)
Maneuvering (section 6.2)	Torque controller	Velocity controller
Stabilization (section 7.2)	Velocity controller	—

Among the differing applications of these robotic tails, a commonality among them is their structure. Each of the tails referred to above consist of a single-link pendulum designed to operate with either one-DOF [10, 11, 13–15, 17, 19] or two-DOF [12, 14, 18]. None of the tail structures demonstrated by other authors directly adapted the articulated structure of a biological tail into their designs.

As an alternative to the single-link pendulum approach, bioinspired articulated tails have been considered by the authors. Thus far, three designs of serpentine articulated tails have been presented [7, 8, 20], along with prior work analyzing the benefits this type of tail structure can provide in relation to single-link tails [6, 21]. Additional details on prior work in robotic tails can be found in [22].

2.2. Hyper redundant robot control

Since the prior work associated with the control of articulated tails has been published by the authors [23, 24], prior work in the control of cantilevered hyper redundant robots (both serpentine and continuum) was consulted to guide this work; work focused on the use of serpentine and continuum robotic structures for snake-like locomotion differed too greatly from the use of the robotic structure as a tail.

The clearest delineation of controllers for hyper redundant robots [25] is whether or not they utilize a model of the hyper redundant structure (either kinematic or dynamic) in the formulation of the control laws. Model-free controllers are typically built on conventional approaches including PID controllers [26, 27] and neural networks [28, 29]. The benefit of these types of approaches are their simplicity: given a model or prototype, the PID gains can be tuned or the neural network trained and only simple, model-free calculations are needed in real-time to achieve the desired behavior.

Model-based controllers build on the feedback-based model-free approaches by incorporating additional sources of data based on the known kinematics or dynamics of the structure being controlled. A kinematic model of the hyper redundant robot (specifically, the Jacobian) can be used to map sensor data in the robot's task space into the joint space being controlled [30–32]. The known system dynamics of a robotic structure can also be incorporated into a controller design to aid in damping undesired vibrations along the structure [33].

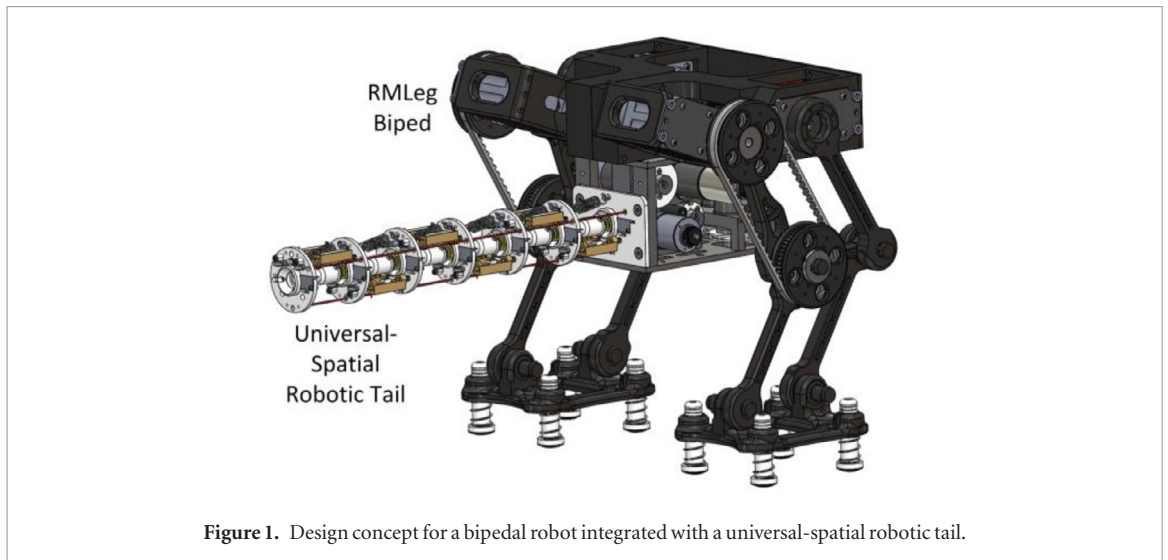


Figure 1. Design concept for a bipedal robot integrated with a universal-spatial robotic tail.

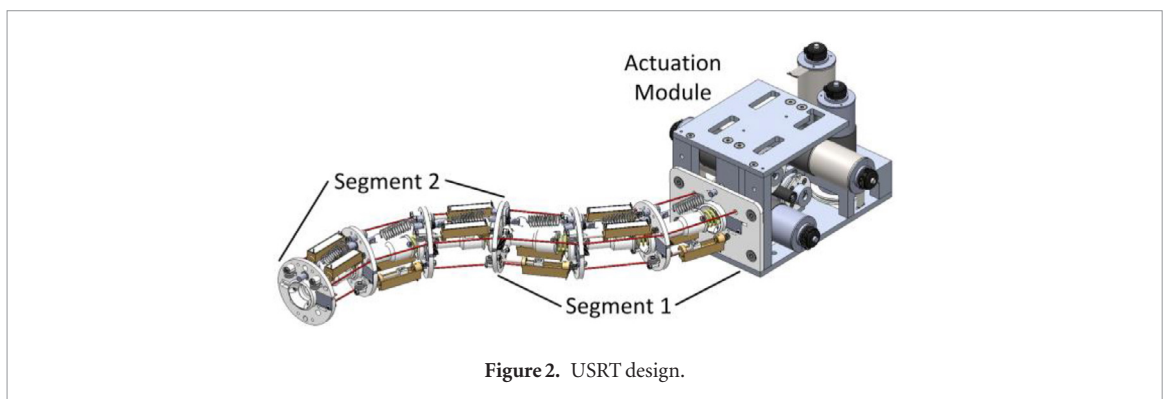


Figure 2. USRT design.

3. Universal-spatial robotic tail (USRT)

The tail subsystem applies the authors' prior works on the USRT [8]. This section details the mechanical design of USRT (section 3.1), along with the dynamic model used to represent it in simulation (section 3.2).

3.1. Tail design

The USRT, shown in figure 2, consists of six similar tail links serially connected to one another and the actuation module by universal joints. These universal joints allow for relative pitch and yaw between adjacent links while constraining their relative roll. A joint angle limit is incorporated into the link design to limit the maximum angular deflection of the universal joint from its straight configuration to 35° in any direction.

The actuation module houses six gearmotors used to actuate the USRT. A spool is mounted to the output shaft of each gearmotor, and a cable routed along the USRT is wrapped around this spool. These six cables are used to create two quasi-independently actuated segments in the USRT. Segment 1 consists of links 1–3, and is created by terminating (i.e. tying off) three of the cables at disk 3. Segment 2 is comprised of links 4–6, and the remaining three cables terminate at disk 6. The cable routing holes passing through each disk are a fixed distance r_h from the disk center, and are equally

spaced radially at 120° . Since the segment 2 cabling passes through segment 1, the segment 2 cables' tensions will impact the segment 1 dynamics; however, to simplify the dynamics, the two sets of cables route through the same holes.

Between each pair of adjacent links, two sources of elastic loading are present. A compression spring surrounding the universal joint is housed between the links to equally resist bending in all directions. Functionally, this spring helps distribute the motion of the joints within an actuated segment so that deflection is not localized within only one or two joints. An extension spring is attached to the two adjacent disks above the universal joint to provide additional pitch moment in the universal joint. Functionally, this spring helps to counteract gravity and reduce the actuation required to hold the tail in a cantilevered configuration.

Two types of sensors are incorporated into the tail design to help estimate the universal joint angles and velocities, as discussed in section 5.1. For each universal joint 1–6, a pair of distance sensors (12 total) are mounted to fixed points between the disks surrounding the universal joint. For each link 0–7, an inertial measurement unit (IMU) is mounted to measure the links' body-frame angular velocities.

Additional detail on the design of the USRT can be found in [8].

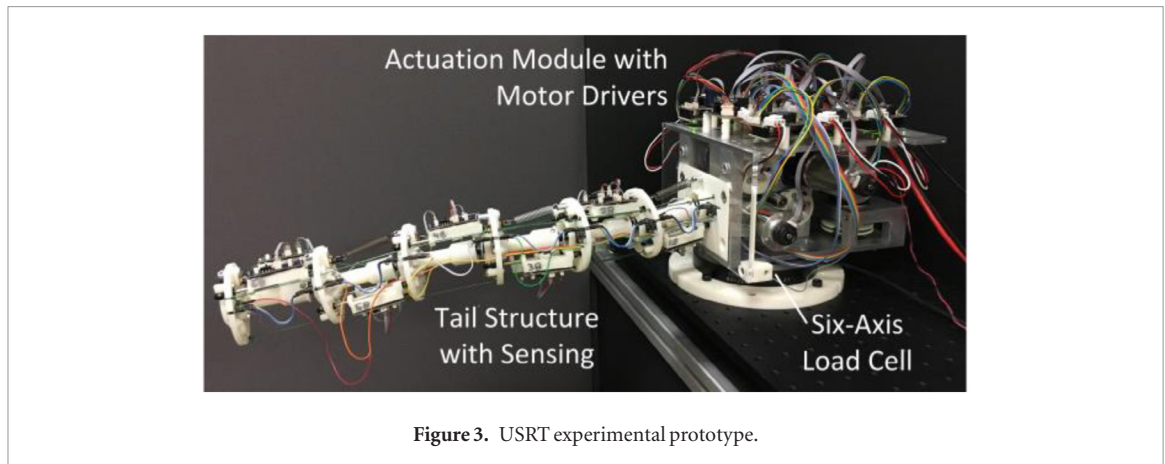


Figure 3. USRT experimental prototype.

3.2. Tail model

The six universal joints lead to a 12-DOF joint workspace consisting of the vectors of the joints' pitch angles $\phi \in \mathbb{R}^6$ and yaw angles $\theta \in \mathbb{R}^6$. For universal joint $i \in \{1, \dots, 6\}$, ϕ_i is the joint i pitch angle and θ_i is the joint i yaw angle. Using these pitch and yaw vectors, the system's state vector $\mathbf{q} = [\boldsymbol{\phi}^T \ \boldsymbol{\theta}^T]^T$ may be formulated.

The six actuation cables provide six cable tension inputs to the dynamic system that may be collected in the vector $\mathbf{T} \in \mathbb{R}_{\geq 0}^6$. The k th tension T_k of \mathbf{T} is defined as $k = 3(s - 1) + c$ for cable $c \in \{1, 2, 3\}$ terminating in segment $s \in \{1, 2\}$. The values of the cable tensions are restricted to the domain $T_k \geq 0$ as cables cannot support compressive loads.

The tail's 12 dynamic equations of motion (For more details, refer to [8]) may be represented by equation (1), where $\mathbf{M}(\mathbf{q})$ is the inertia matrix, $\mathbf{C}(\mathbf{q}, \dot{\mathbf{q}})\dot{\mathbf{q}}$ is the Coriolis and centripetal loading vector, $\mathbf{D}\dot{\mathbf{q}}$ is the joint damping loading, $\mathbf{k}(\mathbf{q})$ is joint coupling loading, $\mathbf{g}(\mathbf{q})$ is the gravitational loading, and $\mathbf{F}(\mathbf{q})\mathbf{T}$ is the actuation transmission matrix.

$$\mathbf{M}(\mathbf{q})\ddot{\mathbf{q}} + \mathbf{C}(\mathbf{q}, \dot{\mathbf{q}})\dot{\mathbf{q}} + \mathbf{D}\dot{\mathbf{q}} + \mathbf{k}(\mathbf{q}) + \mathbf{g}(\mathbf{q}) = \mathbf{F}(\mathbf{q})\mathbf{T}. \quad (1)$$

These terms are constructed by considering the moment generated by each loading effect at each joint, and projecting this moment onto the joint's pitch and yaw axes. For the inertial loading $\mathbf{M}\ddot{\mathbf{q}}$ and $\mathbf{C}\dot{\mathbf{q}}$ and gravitational loading \mathbf{g} , the forces and moments acting at the link COMs 'downstream' of each joint (e.g. links 4–6 for joint 4) are mapped into their equivalent moments at the joint and added together.

For the dampening loading $\mathbf{D}\dot{\mathbf{q}}$, estimated Coulomb dampening in each joint is organized into the \mathbf{D} matrix. For the coupling loading \mathbf{k} , three sources contribute: (1) a coaxial force pair due to the extension spring that induces a moment in the universal joint, (2) a pure moment within the universal joint due to the angular deflection of the compression spring, and (3) a nonlinear torsional spring that mimics the contact forces generated by the joint's angle limit when the universal joint deflection exceeds 35° .

For the actuation loading, \mathbf{F} maps the input cable tensions into their equivalent joint moments. This state-dependent matrix changes with \mathbf{q} to represent the changing relative geometry between the cabling and joints.

In addition to the state vector \mathbf{q} , an additional state vector $\mathbf{z} \in \mathbb{R}^4$ is defined in equation (2) in terms of the segment i net pitch ψ_i and yaw η_i bending angles, where $\mathbf{1}_{1 \times 3}$ is a 1-by-3 row vector of ones and $\mathbf{0}$ is an appropriately sized vector of zeros. The three cables used to actuate each segment only allow for control of two DOFs [34]; ψ_i and η_i for segment $i \in \{1, 2\}$ parameterize the controllable workspace of the tail.

$$\mathbf{z} = \begin{bmatrix} \psi_1 \\ \psi_2 \\ \psi_3 \\ \psi_4 \end{bmatrix} = \boldsymbol{\mu}\mathbf{q} = \begin{bmatrix} \mathbf{1}_{1 \times 3} & \mathbf{0} & \mathbf{0} & \mathbf{0} \\ \mathbf{0} & \mathbf{1}_{1 \times 3} & \mathbf{0} & \mathbf{0} \\ \mathbf{0} & \mathbf{0} & \mathbf{1}_{1 \times 3} & \mathbf{0} \\ \mathbf{0} & \mathbf{0} & \mathbf{0} & \mathbf{1}_{1 \times 3} \end{bmatrix} \mathbf{q}. \quad (2)$$

Furthermore, although the universal joints does not allow for relative roll between links, a rolling tail motion can be generated by coordinating the motion of the joints' yaw and pitch angles. To parameterize this motion, three additional variables are introduced: a bending plane angle ξ , and two segment bending angles β_1 (joints 1–3) and β_2 (for joints 4–6). An implicit relationship between $\{\xi, \beta\}$ and $\{\boldsymbol{\phi}, \boldsymbol{\theta}\}$ is defined by equation (3), and either set of joint angles can be solved from the other subject to the angles' constraints ($\xi \in [-180^\circ, 180^\circ]$, $\beta_j \in [0, 3\beta_{\text{lim}}]$, $\{\phi_i, \theta_i\} \in [-\beta_{\text{lim}}, \beta_{\text{lim}}]$).

$$\mathbf{R}_Z(\xi) \mathbf{R}_Y(\beta_j/3) \mathbf{z} = \mathbf{R}_Y(\phi_i) \mathbf{R}_X(\theta_i) \mathbf{z} \quad (3)$$

$$j = \begin{cases} 1, & i \in \{1, 2, 3\} \\ 2, & i \in \{4, 5, 6\} \end{cases}.$$

3.3. Tail experimental setup

Figure 3 shows the experimental setup used to implement the desired tail motion and measure the associated dynamic loading. This prototype is discussed in detail in [8], and the mass and geometric properties extracted from this prototype and utilized in the simulations are defined in tables 2 and 3. The

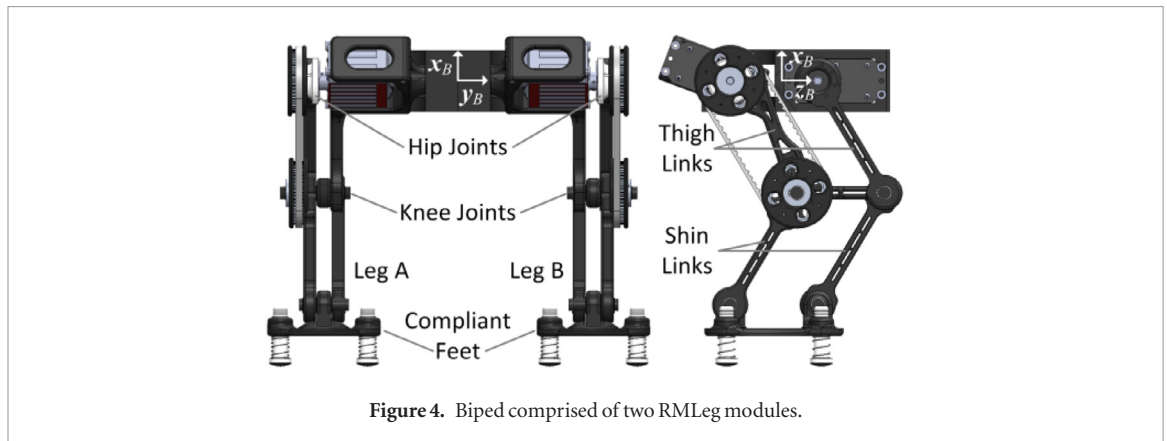


Figure 4. Biped comprised of two RMLeg modules.

Table 2. USRT mass and geometric properties.

Var.	Value	Var.	Value
L_{JJ}	80 mm	$\mathbf{p}_{01,jnt}^{TB}$	$[62.85, 0, 53.5]^T$ mm
L_{JD}	74 mm	$\mathbf{p}_{0,jc}^{TB}$	$[84.64, 0, -56.13]^T$ mm
L_{JC}	46.6 mm	$\mathbf{p}_{ex,B}^i$	$[30.5, 0, 6]^T$ mm
L_{DJ}	6 mm	$k_{i,cp}$	2.82 N m/rad
m_0	6507 g	$c_{i,dmp}$	0.1 N m s/rad
$m_{\{1-6\}}$	85 g	β_{lim}	35 deg.
r_{hl}	32.5 mm	$k_{i,lim}$	100 N m/rad
μ_s	0	$c_{i,lim}$	0.1 N m s/rad

USRT's actuation module is mounted on a six-axis load cell (Sunrise Instruments M3176B) capable of measuring the three components of force and moment applied by the tail through its base to its mounting.

4. Robotic modular leg biped

The biped subsystem applies the authors' prior works on the Robotic Modular Leg (RMLeg) [9]. This section presents the design (section 4.1), model (section 4.2), and motion planning (section 4.3) of the biped used to demonstrate the USRT's maneuvering and stabilization functionalities.

4.1. Biped design

The biped is comprised of a pair of mirrored RMLeg modules coupled together at their hip links, with their feet moving in parallel planes. Each RMLeg's two-DOFs control their foot's relative planar position with respect to the hip. As the leg moves, the mechanism's parallelogram structure of the RMLeg preserves the parallel relative orientation between the hip and the foot.

Figure 4 shows side and rear views of the biped. The thigh four-bar is actuated at the right hip joint by a motor mounted to the hip link. The shin four-bar motor is mounted in the left thigh link, and a 1:1 timing belt transmits its actuation to drive the left shin joint at the knee. Since the shin motor is mounted to

Table 3. USRT mass and geometric properties.

Jnt.	$k_{i,ex}$ (N m ⁻¹)	$L_{i,ex}$ (mm)	$F_{i,ex}$ (N)	$\mathbf{p}_{i,ex,T}^i$ (mm)
1	1460.6	38.354	3.47	[20.8; 0; -14.26]
2	1460.6	38.354	3.47	[20.8; 0; -16.18]
3	684.7	36.830	4.27	[20.8; 0; -13.45]
4	455.3	36.830	2.98	[20.8; 0; -13.39]
5	122.6	37.592	1.02	[20.8; 0; -15.38]
6	122.6	37.592	1.02	[20.8; 0; -15.57]

the thigh and not the hip, the two joint motions are decoupled.

Contact between the foot and the ground is facilitated by four compliant toes incorporated into the foot. Without these toes, since the foot is designed to remain parallel to the hip, minor pitch or roll in the biped could cause loss of planar foot contact during locomotion. As this biped is designed to implement quasi-statically stable gaits, this loss of planar contact would further destabilize the system. The compliant toes extend and retract from their nominal displacement during locomotion to maintain a planar support polygon despite the biped's pitch and roll. However, once a toe reaches its maximum extension or retraction, one or more toes may lose contact.

Note that the biped in figure 4 alone is not able to balance itself during static walking due to the lack of abduction joints. This causes the COM to be outside of the support polygon during the single-leg-stance phase. The biped is designed to work with the tail which helps the biped to adjust its overall COM and thus achieve static walking. Therefore, the term 'quasi-static' refers to the basic assumption for the mobile platform in this paper: the biped is designed to perform traditional static locomotion instead of the more advanced dynamical locomotion. With this assumption, the research problem can be simplified significantly and focuses on the tail functionalities. The term 'quasi' refers to the perturbations and other transient phases when the tail is actively performing the maneuvering and stabilization tasks.

4.2. Biped model

MSC ADAMS is used to model the dynamics of the biped, based on the geometry and mass properties of a 3D CAD model exported from Solidworks. Kinematic constraints are used to prescribe desired joint velocities at the biped's hip and knee joints, and the multi-body dynamics model internally calculates the associated torques required to implement these trajectories.

External loading effects representing ground contact, gravity and tail loading are incorporated into the dynamic model, in addition to the inertial loading effects generated by the CAD's mass and geometric properties. Ground contact at each toe generates a normal force based on a damped elastic model acting against the toe penetrating the ground and a friction force opposing the toe's sliding velocity and calculated using a velocity-dependent friction coefficient to mimic stiction behavior. To mimic the effect of the tail, a rigid-body is fixed to the biped hip to account for the tail's effective mass and inertia, and a force/moment input is used to prescribe the tail's effective loading to the biped.

The mass m_B and moment of inertia tensor \mathbf{I}_B of the biped when standing are defined in equations (4) and (5). The 180mm distance between each hip and knee joint is the same as the distance between each knee and foot joint.

$$m_B = 6.512 \text{ kg} \quad (4)$$

$$\mathbf{I}_B = \begin{bmatrix} 0.1863 & 0.0000 & 0.0003 \\ 0.0000 & 0.1830 & -0.2660 \\ 0.0003 & -0.2660 & 0.1537 \end{bmatrix} \text{ kg} \cdot \text{m}^2. \quad (5)$$

4.3. Biped motion planning

This analysis focuses on controllers that generate maneuvering and stabilization behaviors in a tailed-biped system. As a result, leg motions are planned that demonstrate those behaviors without the need for full-scale demonstration of the biped's steady-state walking ability, which will be addressed in future studies focusing on the tailed-biped as a whole.

For maneuvering, friction at the biped's toes provide a high barrier to overcome to generate meaningful yaw-angle rotation. For bipeds exhibiting dynamically stable gaits with an aerial phase in which neither of the legs are in contact with the ground, friction can be avoided by actuating the tail during this time. For the quasi-statically stable RMLeg biped under consideration, an aerial phase may be mimicked by actuating the legs to generate a jumping or hopping motion.

The hopping motion is generated by actuating the legs in parallel to generate a vertical velocity in the biped, and then discontinuously stopping the leg actuation so that the biped's vertical momentum lifts the biped off the ground. A fifth-order polynomial is used to generate the hopping motion: constraints include two position constraints so that the trajectory starts and ends when the foot is h_S from the hip, two zero-

velocity and zero-acceleration constraints at the start of the trajectory, and a desired biped velocity \dot{h}_H at the end of the trajectory.

For stabilization, the biped's quasi-static trot gait alternates each foot between a support phase, in which the foot is in contact with the ground and pushes the biped forward, and a lift phase, in which the foot is not in contact with the ground and returns to the starting point of its support phase. For the stabilization case study, only the vertical motion of the leg is considered.

During the support phase, a foot remains at a fixed vertical distance h_S relative to the hip. During the lift phase, the foot starts from its fixed vertical distance h_S , reaches its maximum height midway through the lift phase at the distance h_L relative to the hip, and returns to the distance h_S at the end of the lift phase. A seventh-order polynomial is used to interpolate the lift-phase foot trajectory; the seven coefficient constraints are the three position constraints, two zero velocity constraints at the trajectory start and end and two acceleration constraints at the trajectory start and end.

In both cases, an inverse kinematics model of the leg is used to map the foot trajectories into joint trajectories.

5. Formulate the inner-loop controllers for the tail subsystem

This section discusses the state estimates used to map the measured sensor data into joint angles and velocities (section 5.1), and the inner-loop control approaches that can be used to map the desired tail trajectory $\mathbf{q}(t)$ into actuation inputs $\mathbf{T}(t)$ (section 5.2).

5.1. Tail state estimation

As discussed in section 3.1, 12 distance sensors (two per joint) are incorporated into the tail design to indirectly estimate the universal joints' angles, in lieu of trying to incorporate encoders on the universal joints themselves. A closed-form analytical calculation of the joint angles based on subsegment kinematics has been formulated [8], but a linearized model of this calculation would significantly reduce the number of computations required in real-time, enabling improved frequency response of the joint angle sensing.

For joints $i \in \{1, \dots, 6\}$, equation (6) defines a linear relationship between the two distance sensor measurements $d_{sns,i,1}$ and $d_{sns,i,2}$ and the two associated universal joint angles ϕ_i and θ_i .

$$\begin{bmatrix} d_{sns,i,1} \\ d_{sns,i,2} \end{bmatrix} = \mathbf{A}_i \begin{bmatrix} \phi_i \\ \theta_i \end{bmatrix} + \mathbf{B}_i = \begin{bmatrix} A_{i,11} & A_{i,12} \\ A_{i,21} & A_{i,22} \end{bmatrix} \begin{bmatrix} \phi_i \\ \theta_i \end{bmatrix} + \begin{bmatrix} B_{i,1} \\ B_{i,2} \end{bmatrix}. \quad (6)$$

The coefficient matrices A_i and B_i are determined by a kinematics-based analysis in three stages. First, the zero-angle configuration of the joint when $\phi_i = \theta_i = 0$ dictates that the B_i coefficients equal L_S , the nominal length of the distance sensor.

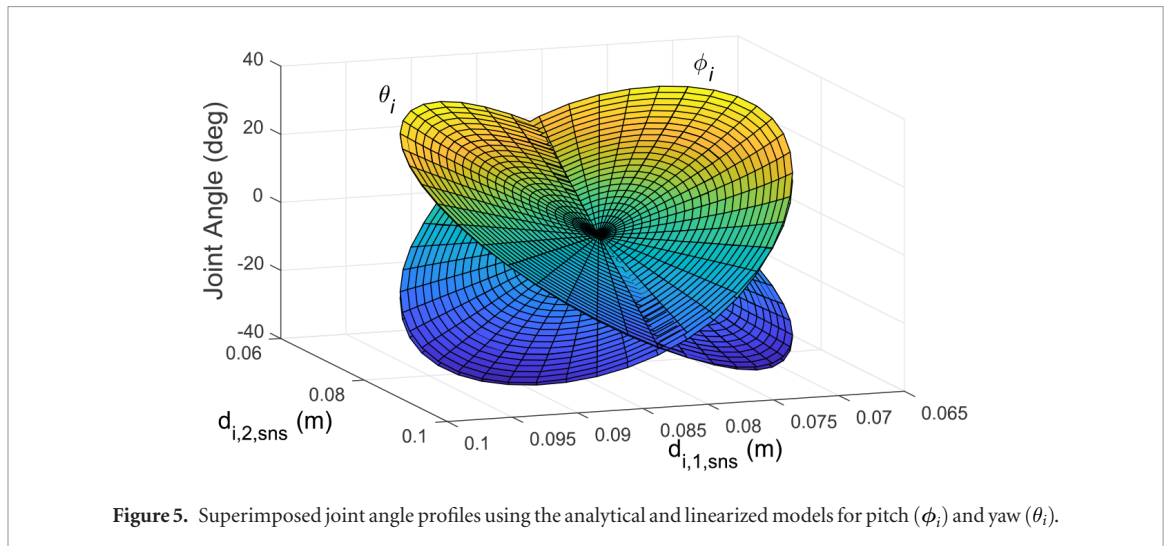


Figure 5. Superimposed joint angle profiles using the analytical and linearized models for pitch (ϕ_i) and yaw (θ_i).

Second, the pitch angle coefficients ($A_{i,11}$ and $A_{i,21}$) over the domain of $\phi_i \in [-\beta_{\text{lim}}, \beta_{\text{lim}}]$ for zero-yaw ($\theta_i = 0$) are calculated using linear regression. Due to the symmetry of the anchor placements, this regression shows that these two coefficients are both equal to a nominal value K_ϕ .

Third, the yaw angle coefficients ($A_{i,12}$ and $A_{i,22}$) are calculated using an array of equally spaced pitch and yaw joint angle pairs within the universal joint workspace. Because of the symmetric placement of the spring anchors with respect to the links' vertical planes and the 90° spacing of the spring anchors, these coefficients are equal and opposite, such that $A_{i,12} = K_\theta$ and $A_{i,22} = -K_\theta$. These calculated coefficients lead to the simplified expressions for calculating ϕ_i and θ_i shown in equation (7).

$$\begin{aligned} \phi_i &= (d_{\text{sns},i,1} + d_{\text{sns},i,2} - 2L_S)/2K_\phi \\ \theta_i &= (d_{\text{sns},i,1} - d_{\text{sns},i,2})/2K_\theta \end{aligned} \quad (7)$$

Comparisons of the analytical and linear calculations of the joint angles using valid distance sensor value pairs within the workspace of the USRT joint are shown in figure 5. Linearization errors in the ranges of -2.01° to 2.66° in the pitch joint and -1.17° to 1.17° in the yaw joint were calculated at the boundaries of the workspace, and average error magnitudes across the total workspace were 0.36° in the pitch joint and 0.19° in the yaw joint.

In addition to the 12 distance sensors, the tail also has seven IMUs to measure the link i body-frame angular velocities ω_i^i . Using the estimates for ϕ_i and θ_i , the link $i-1$ and link i angular velocity measurements ω_{i-1}^{i-1} and ω_i^i can be mapped into $\dot{\phi}_i$ and $\dot{\theta}_i$.

The relative angular velocity between links $i-1$ and i is defined in terms of the link-frame angular velocities in equation (8) and in terms of the joint velocities in equation (9), where $\mathbf{R}_i^{i-1}(\phi_i, \theta_i)$ is the relative orientation between frames $i-1$ and i , \mathbf{y}_{i-1}^{i-1} is the frame $i-1$ y -direction unit vector and \mathbf{x}_i^i is the frame i x -direction unit vector.

$$\omega_{(i-1)i}^{i-1} = \mathbf{R}_i^{i-1} \omega_i^i - \omega_{i-1}^{i-1} \quad (8)$$

$$= \dot{\phi}_i \mathbf{y}_{i-1}^{i-1} + \dot{\theta}_i \mathbf{R}_i^{i-1} \mathbf{x}_i^i \quad (9)$$

Equating equations (8) and (9) and taking the dot products of each side with \mathbf{y}_{i-1}^{i-1} and $\mathbf{R}_i^{i-1} \mathbf{x}_i^i$ result in $\dot{\phi}_i$ and $\dot{\theta}_i$, respectively, as shown in equation (10).

$$\begin{aligned} \dot{\phi}_i &= \omega_{i,y}^i \cos \theta_i - \omega_{i-1,y}^{i-1} - \omega_{i,z}^i \sin \theta_i \\ \dot{\theta}_i &= \omega_{i,x}^i - \omega_{i-1,x}^{i-1} \cos \phi_i + \omega_{i-1,z}^{i-1} \sin \phi_i \end{aligned} \quad (10)$$

5.2. Tail inner-loop control

Two methods for implementing the USRT's inner-loop control have been considered for this analysis: prescribed velocity and prescribed torque. The prescribed velocity method maps the USRT's state velocity trajectory $\dot{\mathbf{q}}(t)$ into a set of cable displacement velocities $\dot{\delta}_{i,j}(t)$ for cable $j \in \{1, 2, 3\}$ terminating in segment $i \in \{1, 2\}$. Based on the properties of the actuation transmission mechanism in the actuation module between the cable spool and motor, these cable velocities can be mapped into motor speed commands.

This inner-loop control approach, which was used in [15], does not require sensing data from the tail; it only requires the incremental encoder feedback from the individual motors, which is then used to estimate the motor speed. Its primary benefit is its simplicity—consideration of the tail dynamics is not needed. When simulating this type of inner-loop controller, the desired tail velocities are applied to the model as kinematic constraints, and Lagrange multipliers analogous to the cable tensions are calculated for each motor.

For prescribed torque inner-loop control, two considerations guide the calculation of the desired $\mathbf{T}(t)$: (1) achieving the desired tail motion defined by $\mathbf{z}_d(t)$ and (2) ensuring each cable maintains a minimum tension T_{min} at all times during the tail motion. As a result, $\mathbf{T} = \mathbf{T}_{\text{act}} + \mathbf{T}_{\text{ten}}$, where \mathbf{T}_{act} is the tail actuation contribution and \mathbf{T}_{ten} is the cable tensioning contribution.

5.2.1. Prescribed torque actuation contribution

Ideally, the feedback linearization controller defined in equation (11) could be used to calculate \mathbf{T}_{act} , where $\hat{\mathbf{a}}$ denotes an estimate of the associated matrix or vector from equation (1), \mathbf{a} is the prescribed outer-loop acceleration and $\hat{\mathbf{V}}(\mathbf{q}, \dot{\mathbf{q}}, \ddot{\mathbf{q}})$ is a vector of the estimated non-actuation loading effects. However, the USRT's underactuation precludes the calculation of \mathbf{T}_{act} using equation (11), as a left inverse cannot be guaranteed to exist for the 12-by-6 $\hat{\mathbf{F}}$ matrix.

$$\hat{\mathbf{F}}\mathbf{T}_{act} = \hat{\mathbf{M}}\mathbf{a} + (\hat{\mathbf{C}} + \hat{\mathbf{D}})\dot{\mathbf{q}} + \hat{\mathbf{k}} + \hat{\mathbf{g}} = \hat{\mathbf{V}}(\mathbf{q}, \dot{\mathbf{q}}, \ddot{\mathbf{q}}). \quad (11)$$

Based on the geometry of the cable actuation, the rank of $\hat{\mathbf{F}}$ can only be guaranteed to be 4 within the tail's workspace (2 of columns 1–3 are linearly independent, 2 of columns 4–6 are linearly independent). To reduce the 12 equations of motions to 4, both sides of equation (11) are multiplied by $\boldsymbol{\mu}$, as shown in equation (12). The $\boldsymbol{\mu}\hat{\mathbf{F}}$ term is now a 4-by-6 matrix of rank 4.

$$\boldsymbol{\mu}\hat{\mathbf{F}}\mathbf{T}_{act} = \boldsymbol{\mu}\hat{\mathbf{V}}. \quad (12)$$

To extract a 4-by-4 matrix from $\boldsymbol{\mu}\hat{\mathbf{F}}$, two of the cable tensions in \mathbf{T}_{act} are set as zero, and the tensions for the remaining four cables A, B, C and D are solved for using equation (13), where \mathbf{T}_{ABCD} is the 4-by-1 vector of non-zero cable tensions from \mathbf{T}_{act} and $\boldsymbol{\mu}\hat{\mathbf{F}}_i$ is the i th column of $\boldsymbol{\mu}\hat{\mathbf{F}}$. The segment 1 cables A and B are defined such that $A \in \{1, 2, 3\}$ and $B \in \{1, 2, 3 \mid B \neq A\}$, and the segment 2 cables C and D are defined similarly for cable indices $\{4, 5, 6\}$.

$$\mathbf{T}_{ABCD} = [(\boldsymbol{\mu}\hat{\mathbf{F}})_A \quad (\boldsymbol{\mu}\hat{\mathbf{F}})_B \quad (\boldsymbol{\mu}\hat{\mathbf{F}})_C \quad (\boldsymbol{\mu}\hat{\mathbf{F}})_D]^{-1} \boldsymbol{\mu}\hat{\mathbf{V}}. \quad (13)$$

At least one set of the nine unique combinations of $\{A, B, C, D\}$ will produce an actuating tension vector for which each of the cable tensions $\mathbf{T}_{act} \geq 0$, satisfying the constraint that cables cannot support a compressive load.

5.2.2. Prescribed torque tensioning contribution

Since the calculation of \mathbf{T}_{act} by definition prescribes at least two cable tensions as zero, a methodology for uniformly scaling up the prescribed cable tensions without changing the dynamic behavior of the tail is needed. This is done by exploiting the null space of $\boldsymbol{\mu}\hat{\mathbf{F}}$ due to the matrix's rank deficiency.

Like the analysis in section 5.2.1, the 12-by-6 $\hat{\mathbf{F}}$ cannot be used directly to calculate \mathbf{T}_{ten} using $\hat{\mathbf{F}}\mathbf{T}_{ten} = \mathbf{0}$; as shown in equation (14), $\boldsymbol{\mu}$ is used to consider the impact of the actuation on the tail's pitch and yaw bending. This results in a $\hat{\mathbf{F}}\mathbf{T}_{ten}$ vector that is not identically equal to zero, but may be approximated as such.

$$\boldsymbol{\mu}\hat{\mathbf{F}}\mathbf{T}_{ten} = \mathbf{0} \Rightarrow \hat{\mathbf{F}}\mathbf{T}_{ten} \approx \mathbf{0}. \quad (14)$$

The rows of matrix $\boldsymbol{\mu}\hat{\mathbf{F}}$ may be rearranged as shown in equation (15), where $(\boldsymbol{\mu}\hat{\mathbf{F}})_{ij}$ is the 1-by-3

row i vector for the segment j cables, $\mathbf{T}_{ten,1:3}$ is the vector of segment 1 cable tensions and $\mathbf{T}_{ten,4:6}$ is the vector of segment 2 cable tensions.

$$\begin{bmatrix} (\boldsymbol{\mu}\hat{\mathbf{F}})_{1,1} & (\boldsymbol{\mu}\hat{\mathbf{F}})_{1,2} \\ (\boldsymbol{\mu}\hat{\mathbf{F}})_{3,1} & (\boldsymbol{\mu}\hat{\mathbf{F}})_{3,2} \\ \mathbf{0} & (\boldsymbol{\mu}\hat{\mathbf{F}})_{2,2} \\ \mathbf{0} & (\boldsymbol{\mu}\hat{\mathbf{F}})_{4,2} \end{bmatrix} \begin{bmatrix} \mathbf{T}_{ten,1:3} \\ \mathbf{T}_{ten,4:6} \end{bmatrix} = \begin{bmatrix} \mathbf{0} \\ \mathbf{0} \end{bmatrix}. \quad (15)$$

For the segment 2 cable tensions, rows 3 and 4 from equation (15) may be reformulated as $(\boldsymbol{\mu}\hat{\mathbf{F}})_2 \mathbf{T}_{ten,4:6} = \mathbf{0}$, where $(\boldsymbol{\mu}\hat{\mathbf{F}})_2$ is the 2-by-3 segment 2 actuation transmission matrix. The unit vector $\hat{\mathbf{T}}_{ten,4:6}$ is the basis of the null space of $(\boldsymbol{\mu}\hat{\mathbf{F}})_2$, and its magnitude $|\mathbf{T}_{ten,4:6}|$ is scaled such that the minimum segment 2 cable tension $\mathbf{T}_{4:6} = \mathbf{T}_{act,4:6} + \mathbf{T}_{ten,4:6}$ equals the minimum desired cable tension T_{min} .

For the segment 1 cable tensions, rows 1 and 2 from equation (15) may be further simplified based on the knowledge that the segment 1 and 2 cables route through the same holes in segment 1. Therefore, $(\boldsymbol{\mu}\hat{\mathbf{F}})_{\{1,3\},1} = (\boldsymbol{\mu}\hat{\mathbf{F}})_{\{1,3\},2}$, and the 2-by-3 segment 1 actuation transmission matrix $(\boldsymbol{\mu}\hat{\mathbf{F}})_1$ may be defined using equation (16) based on rows 1 and 2 from equation (15).

$$(\boldsymbol{\mu}\hat{\mathbf{F}})_1 (\mathbf{T}_{ten,1:3} + \mathbf{T}_{ten,4:6}) = \mathbf{0}. \quad (16)$$

Since the segment 2 cabling routes through segment 1, their effect must be accounted for when calculating $\mathbf{T}_{ten,1:3}$. For this segment, the unit basis of the $(\boldsymbol{\mu}\hat{\mathbf{F}})_1$ null space is no longer the unit vector $\hat{\mathbf{T}}_{ten,1:3}$, but rather the unit vector of the sum $\mathbf{T}_{ten,12} = \mathbf{T}_{ten,1:3} + \mathbf{T}_{ten,4:6}$. Therefore, the magnitude $|\mathbf{T}_{ten,12}|$ should be selected to ensure that the minimum segment 1 cable tension $\mathbf{T}_{1:3} = \mathbf{T}_{act,1:3} + \mathbf{T}_{ten,1:3}$ equals the minimum desired cable tension T_{min} . As an intermediate step, $\mathbf{T}_{ten,1:3}$ is calculated using equation (17), based on the prescribed $|\mathbf{T}_{ten,12}|$.

$$\mathbf{T}_{ten,1:3} = |\mathbf{T}_{ten,12}| \hat{\mathbf{T}}_{ten,12} - \mathbf{T}_{ten,4:6} \quad (17)$$

5.2.3. Prescribed torque stability

In this analysis, it will be assumed that the estimated tail model vectors and matrices exactly match the actual tail dynamics ($\hat{\mathbf{M}} = \mathbf{M}$, $\hat{\mathbf{F}} = \mathbf{F}$, etc). As a result, equations (11) and (14) may be re-formulated using \mathbf{F} and substituted into equation (1) to calculate the closed-loop system defined by equation (18).

$$\hat{\mathbf{M}}\ddot{\mathbf{q}} + (\mathbf{C} + \mathbf{D})\dot{\mathbf{q}} + \mathbf{k} + \mathbf{g} = \hat{\mathbf{M}}\mathbf{a} + (\hat{\mathbf{C}} + \hat{\mathbf{D}})\dot{\mathbf{q}} + \hat{\mathbf{k}} + \hat{\mathbf{g}}. \quad (18)$$

As desired, the tensioning contribution to the controller does not impact the closed-loop dynamics, and the feedback linearization controller reduces the nonlinear open-loop dynamics into the linear double-integrator $\ddot{\mathbf{q}} = \mathbf{a}$. Since \mathbf{T}_{act} acts to control the reduced-state \mathbf{z} and not the full-state \mathbf{q} , the system sta-

bility will be defined with respect to \mathbf{z} . The prescribed outer-loop acceleration \mathbf{a} is defined in equation (19), where \mathbf{K}_0 and \mathbf{K}_1 are proportional and derivative control gain matrices, respectively.

$$\mathbf{a} = \frac{1}{3}\boldsymbol{\mu}^T \left(\ddot{\mathbf{z}}_d - \mathbf{K}_0\tilde{\mathbf{z}} - \mathbf{K}_1\dot{\tilde{\mathbf{z}}} \right). \quad (19)$$

Substituting equation (19) into (18) and multiplying both sides of the equation by $\boldsymbol{\mu}$ results in the closed-loop dynamics represented in the canonical form shown in equation (20). Stability for this type of system is guaranteed as long as \mathbf{K}_0 and \mathbf{K}_1 are positive definite.

$$\ddot{\tilde{\mathbf{z}}} + \mathbf{K}_1\dot{\tilde{\mathbf{z}}} + \mathbf{K}_0\tilde{\mathbf{z}} = 0. \quad (20)$$

Note that the computed torque controller developed in this section consists of two parts: the feedback part takes tail measurements into consideration and the feedforward part accelerates the control efforts by adding the precomputed torque based on the inverse dynamics. Therefore, although the dynamic modeling is not accurate, the feedback part (the PD controller defined by \mathbf{K}_0 and \mathbf{K}_1 in equation (20)) is able to compensate the uncertainty/deviation automatically. This control structure is widely used in industrial robots and proved to be robust.

5.3. Discussion on coupling deficiency induced by the decoupled controller

The developed controller in this section only utilized the tail subsystem dynamics which is established based on a fixed base assumption. However, in the actual biped-tail model, the tail base is floating, thus the two subsystems dynamics cannot be decoupled. Therefore, to justify the reliability of the results, it is necessary to discuss and evaluate the coupling deficiency induced by the decoupled controller between the two subsystems.

For the purpose of this discussion, a planar model is utilized as an analogical model of the maneuvering case study in this paper, which refers to the turning action in the sagittal plane while the biped is airborne. Figure 6 illustrates two sagittal models for the tail-biped system. The left model captures the dynamics when the biped is moving (for this case, the tail base is floating on a frictionless plane freely) while the right one captures the assumption used in this paper (that the tail base is fixed). The dynamics for the fix base model is

$$\tau = m_2 r^2 \ddot{\theta}_2. \quad (21)$$

The feedback controller as in equation (20) based on equation (21) is

$$\tau = m_2 r^2 \ddot{\theta}_{2d} - m_2 r^2 (k_1 \dot{e} + k_0 e) \quad (22)$$

where the first term represents the feedforward torque and the second term represents the feedback torque $e = \theta_2 - \theta_{2d}$. The dynamics of the float base model can be represented by

$$\mathbf{M}\ddot{\mathbf{q}} + \mathbf{C}\dot{\mathbf{q}} = \mathbf{B}\boldsymbol{\tau} \quad (23)$$

where $\mathbf{q} = [x \ y \ \theta_1 \ \theta_2]^T$ and the output feedback linearized controller (tracking the same θ_{2d}) for this underactuated system is

$$\tau = I_2 \ddot{\theta}_{2d} + C_2 - I_2 (k_1 \dot{e} + k_0 e) \quad (24)$$

where

$$I_2 = 1 / ([0 \ 0 \ 0 \ 1] \mathbf{M}^{-1} \mathbf{B})$$

$$C_2 = I_2 [0 \ 0 \ 0 \ 1] \mathbf{M}^{-1} \mathbf{C} \dot{\mathbf{q}}.$$

Apparently, the controller in equation (22) is different from the controller defined by equation (24). Since the detailed expressions are too complicated to write down, numerical computations are used to provide qualitative intuitions. For instance, by using the actual parameters in this paper, at the initial position, $I_2 = 0.0213 \text{ kg} \cdot \text{m}^2$ and $C_2 = 0 \text{ N} \cdot \text{m}$. Since I_2 has the same physical meaning as the $m_2 r^2$ (which is $0.0288 \text{ kg} \cdot \text{m}^2$) term in equation (22), the closeness of I_2 and $m_2 r^2$ implies that the controller based on the fixed base model (equation (22)) is qualitatively close to the controller based on the float base model (equation (24)).

Therefore, by using the fixed base model, the decoupled controller introduces a coupling deficiency. However, this coupling deficiency is relatively small compared to the actual control effort. In addition, the missed control effort can be compensated by the PD controller in the feedback loop (k_0 and k_1). Therefore, the controller defined by equation (22) is still reliable. Note that the computation in this section only anecdotally shows the decoupled controller deficiency. The actual control deficiency remains unjustified, which leads to an interesting and necessary analysis on the unified dynamics incorporating both the biped subsystem and the tail subsystem.

6. Maneuvering control

This section describes the maneuvering controller designed to bend the USRT to generate yaw rotation in the biped (section 6.1), along with the results of a case study that implements this controller design on a virtual biped simulation (section 6.2).

6.1. Maneuvering controller design

For the maneuvering task, since it does not require real time response, it is more like the traditional trajectory tracking control of a manipulator. Therefore, the control strategy is chosen to be a prescribed velocity trajectory and a computed torque controller for tracking this trajectory. The feedforward inverse dynamics is taken into account for compensating the feedback control effort.

As discussed in section 4.3, to avoid the need for the tail to act against friction at the biped's feet, tail-based maneuvering will occur while the biped is airborne. To generate yaw rotation in the biped, a yaw-angle tail motion is prescribed, with segments 1 and 2 con-

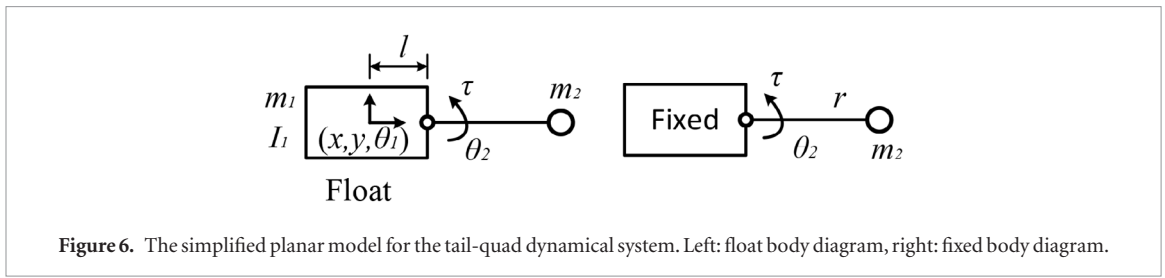


Figure 6. The simplified planar model for the tail-quad dynamical system. Left: float body diagram, right: fixed body diagram.

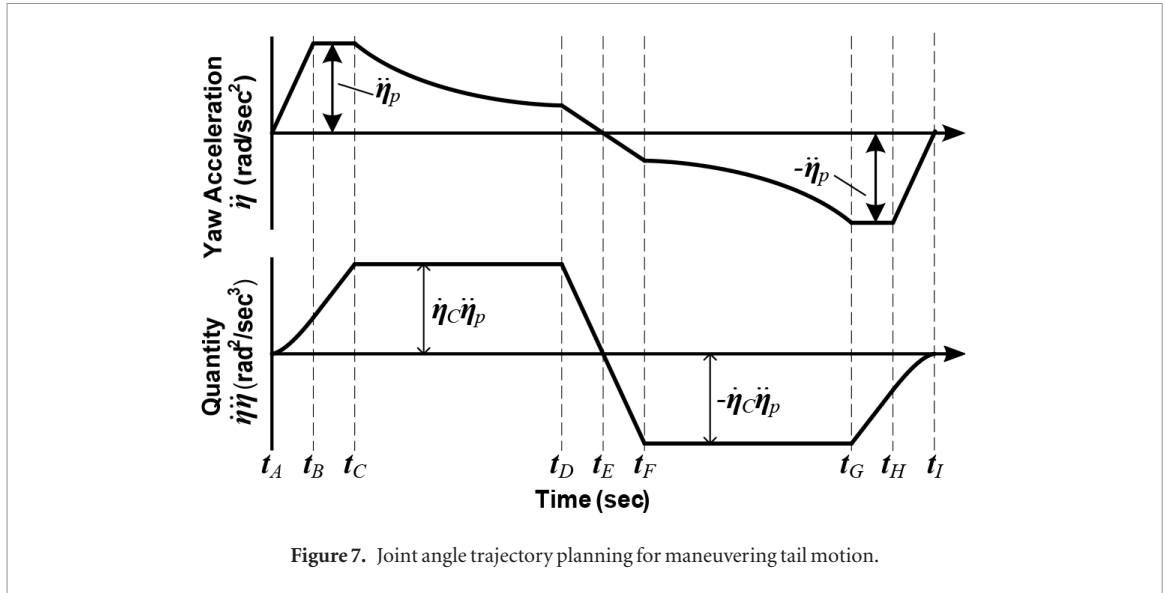


Figure 7. Joint angle trajectory planning for maneuvering tail motion.

strained so that $\eta_1 = \eta_2 = \eta$ and $\psi_1 = \psi_2 = 0$. In this analysis, the desired η trajectory is calculated by defining an acceleration trajectory and integrating from initial conditions η_A and $\dot{\eta}_A$. Specifically, the $\ddot{\eta}$ trajectory is defined as a piecewise continuous function in equation (25) and shown in figure 7, where $t_{\{A, \dots, I\}}$ are sequential time points along the trajectory, $\ddot{\eta}_p$ is the peak η acceleration and $\dot{\eta}_C = \dot{\eta}(t_C)$.

$$\ddot{\eta} = \begin{cases} \ddot{\eta}_p \frac{t-t_A}{t_B-t_A} & t_A \leq t \leq t_B \\ \ddot{\eta}_p & t_B \leq t \leq t_C \\ \ddot{\eta}_p \frac{\dot{\eta}_C}{\dot{\eta}} & t_C \leq t \leq t_D \\ \ddot{\eta}_p \frac{\dot{\eta}_C}{\dot{\eta}} \frac{t_E-t}{t_E-t_D} & t_D \leq t \leq t_E \\ -\ddot{\eta}_p \frac{\dot{\eta}_C}{\dot{\eta}} \frac{t-t_E}{t_F-t_E} & t_E \leq t \leq t_F \\ -\ddot{\eta}_p \frac{\dot{\eta}_C}{\dot{\eta}} & t_F \leq t \leq t_G \\ -\ddot{\eta}_p & t_G \leq t \leq t_H \\ -\ddot{\eta}_p \frac{t-t}{t_I-t_H} & t_H \leq t \leq t_I \end{cases} \quad (25)$$

The $\ddot{\eta}$ trajectory is defined in this manner to reduce the peak cable tensions required to actuate the maneuvering tail motion. As shown in figure 7, higher magnitude accelerations are biased toward the beginning and end of the trajectory, when $|\dot{\eta}|$ is low. In the timespans $[t_C, t_D]$ and $[t_F, t_G]$, $\ddot{\eta}$ is defined to maintain a constant product $\dot{\eta}\ddot{\eta} = \dot{\eta}_C\ddot{\eta}_p$, as shown in figure 7. This product is a kinematic analogue to the motor power required to generate the tail motion's inertial loading; other approaches show significant motor power peaks when high torques are required when the motor is operating at increased speed.

In addition, there is a linear relationship between the net tail displacement $\Delta\eta = \eta_I - \eta_A$ and $\ddot{\eta}_p$; greater $\Delta\eta$ tail motions correlate to higher biped yaw-angle rotations, providing a means of determining $\ddot{\eta}_p$ to generate a desired biped rotation.

6.2. Maneuvering case study

For the maneuvering case study based on simulated tail loading results, the prescribed torque inner-loop controller is utilized, since it incorporates feedforward consideration of the tail dynamics and feedback consideration of the tail measurements. To better simulate the real system and test the stability of the controller, two types of uncertainty are introduced into the system. The first source of uncertainty comes from the inaccuracy of state measurements. For this part, a band-limited white noise with 5×10^{-7} power and 0.5 ms sample time (whose standard deviation is around 10% of the state value) is added on \mathbf{q} only since $\dot{\mathbf{q}}$ is estimated based on \mathbf{q} from equations (8)–(10). The second source of uncertainty comes from the modeling inaccuracy which is assumed mainly due to the friction model of the USRT. For the current version of the USRT dynamics, two types of friction are considered [8]. One is the viscosity damping associated with the joint rotations and the other is the belt friction associated with the cable routings. However, both frictions turn out to be highly nonlinear and the two models cannot predict the actual friction forces accurately (for instance, the belt friction model assumes a perfect round contact between the cable

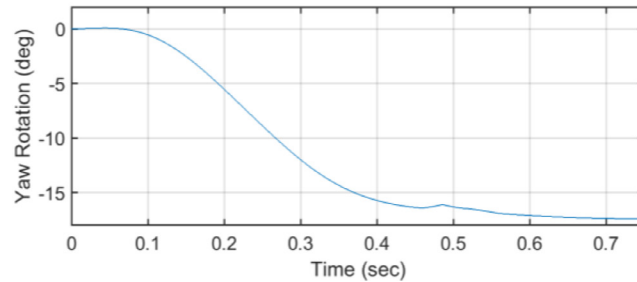


Figure 8. Simulated biped yaw angle trajectories due to simulated tail loading profiles. (Generated by ADAMS/MATLAB Co-simulation).

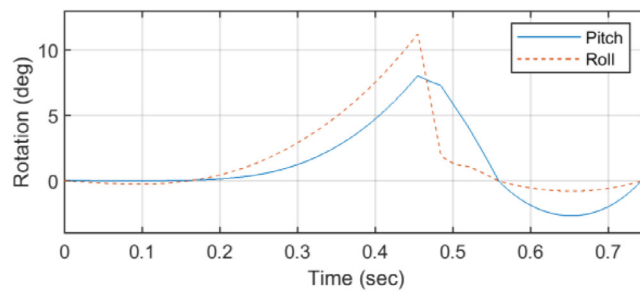


Figure 9. Simulated biped pitch and roll angle trajectories due to simulated tail loading profiles. (Generated by ADAMS/MATLAB Co-simulation).

and the object while the actual cable performs very complicated contacts with the object). Therefore, a white noise with 1×10^{-5} power and 0.5 ms sample time (whose standard deviation is around 5% of the average cable tensions) is necessary to be added into the cable tensioning force. All offline measured terms (inertia, spring stiffness and dimensional measurements) are assumed to be accurate.

Figure 8 illustrates the change in yaw-angle heading due to a yaw-angle bending of 90° in segments 1 and 2, and figure 9 shows the biped's pitch and roll angle trajectories due to the maneuvering tail motion. Of particular importance for the biped is the pitch behavior, as the biped lacks the fore legs of a quadruped to help prevent forward tipping. As shown, the tail loading does not introduce instabilities to its auxiliary DOFs.

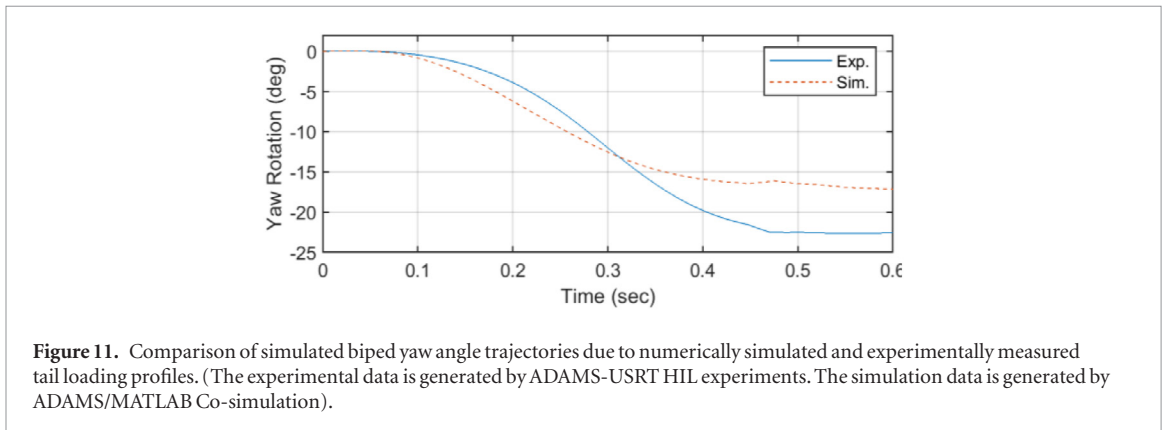
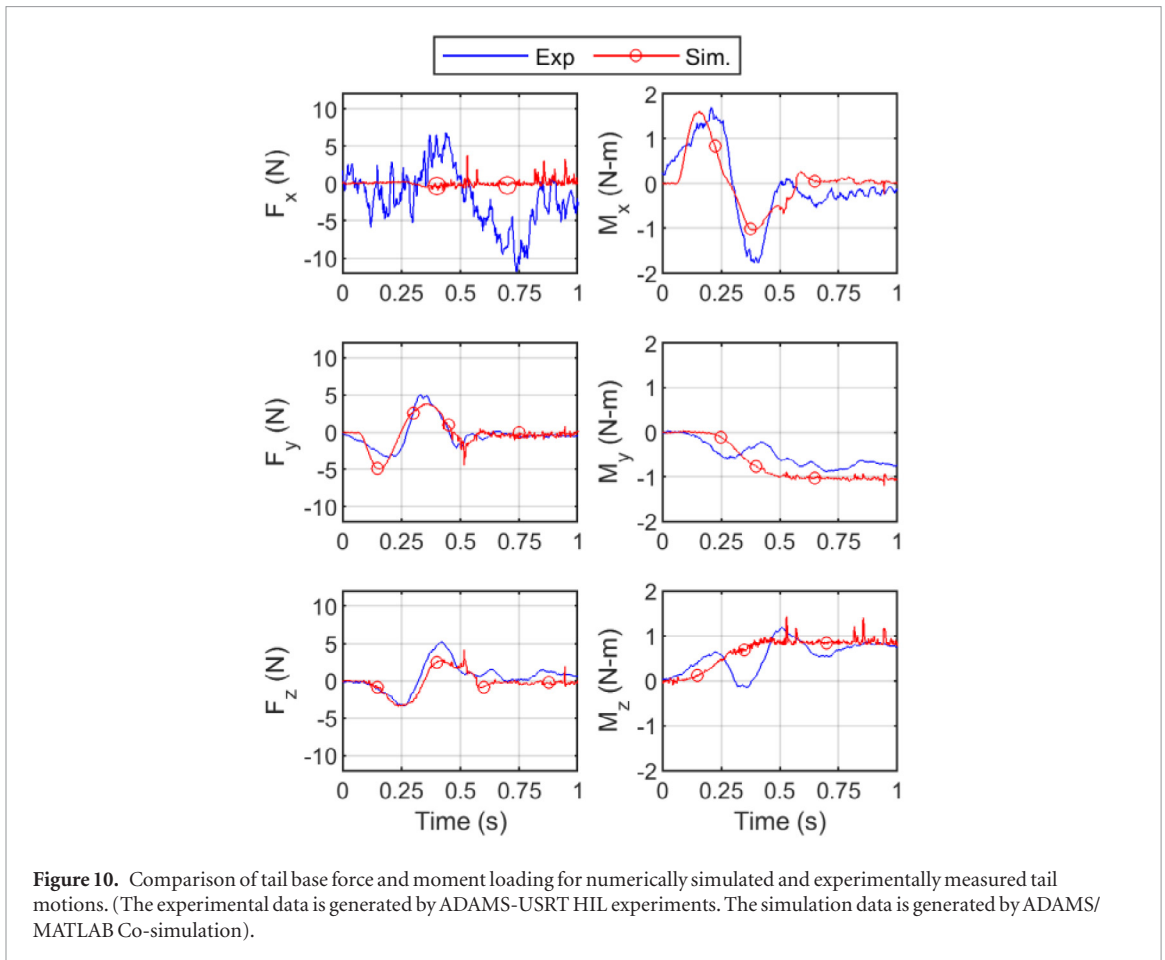
For the maneuvering case study based on experimental tail loading results, the prescribed velocity inner-loop controller is utilized, due to present limitations in implementing the prescribed torque controller on the current generation of the USRT hardware. Results for this case study are compared to the simulated results using the prescribed torque controller.

Figure 10 compares the simulated and experimentally measured loading generated by the maneuvering tail motion. For yaw-angle turning, the x-component of moment is the most critical in dictating the performance of the tailed-biped. As seen, the simulated and experimental results reach a similar maximum value, with a slight delay in the experimental results; however, there is a pronounced

difference in the peak magnitude of the negative moment trajectories. Furthermore, the initial positive moment in the experimental result is applied over a wider timespan than the initial positive moment of the simulated results, implying a greater peak velocity was reached in the experimental tail motion than in the simulated tail motion. The mean error for each force component are computed as 3.53 N, 0.71 N, 0.90 N, 0.39 N · m, 0.28 N · m, 0.25 N · m, corresponding to F_x , F_y , F_z , M_x , M_y , M_z respectively.

Figure 11 compares the simulated biped yaw-angle rotation due to the simulated and experimentally measured tail loading. The effect of the higher-magnitude negative moment in the experimentally measured tail loading is seen clearly in these results: the yaw-angle rotation of the biped is prematurely retarded due to its higher magnitude, resulting in an approximately 5.5° error in the final biped rotation. The increased tail speed in the experimental results initially caused the biped rotation due to the experimental loading to exceed the biped rotation due to the simulated loading, but this excess speed necessitated hard braking by the prescribed velocity controller, which contributed to the error observed.

From figures 10 and 11, it is obvious that the HIL experiment generates similar behaviors as the simulation. This justifies the effectiveness of the HIL approach in the tail-biped research. However, since the tail base was kept stationary in the HIL experiment (which is not true for an actual moving biped-tail robot), the HIL approach introduces a nonnegligible coupling deficiency which is reflected in the



mismatches between the experiment data and the simulation data. Besides the coupling deficiency, the mismatch also contains the modeling inaccuracy (for instance, the elastic and the friction components are highly nonlinear and usually hard to model accurately) for the physical system and the measurement noises from the force sensor.

7. Stabilization control

This section describes the controller used to stabilize the biped's roll-rotation when one of its legs is lifted (section 7.1), and the simulated behavior of the stabilization controller in conjunction with simulations of the tail and biped (section 7.2).

7.1. Stabilization controller design

For the stabilization task, since the controller needs to respond to the disturbances in real time, the precomputed inverse dynamics in the feedforward loop does not help much. Moreover, including the complicated dynamics computation in the feedback loop reduces the working frequency and may only provide marginal benefits. Therefore, the control strategy for the stabilization task is chosen to be a velocity loop control to directly track the desired real time tail behaviors.

Because the RMLeg biped is comprised of a pair of mirrored RMLeg modules, the y component of the biped COM in its local frame is always 0, i.e. the COM lies on the plane $\mathbf{x}_B - \mathbf{z}_B$. Since the RMLeg's feet/toes

do not extend across this plane, the effective gravitational force acting at the biped COM will generate a non-zero rolling moment with respect to the inner edge of the support polygon of the foot in its support phase. In addition, the vertical acceleration of the lift phase foot induces an additional undesired inertial roll moment with respect to the same support polygon edge. These moments induce undesired roll rotation during the steady-state locomotion of the biped. However, the tail can be used to generate cyclic loading during steady-state locomotion to act against this destabilizing moment and maintain a more consistent biped roll.

The tail generates two types of loading that may be used to oppose this destabilizing moment: inertia and gravity. In terms of inertia, a tail rolling motion accelerating in the direction of the roll destabilization will induce a moment opposing the roll destabilization in the biped. In terms of gravity, the tail configurations with maximum gravitational loading opposed to the destabilizing moments are defined in equation (26).

$$\mathbf{z}_{grv,max} = [0, 0, \pm 90^\circ, 0]^T. \quad (26)$$

To illustrate: when leg A (rear view, figure 4) is in its lift phase and leg B is in its support phase, the roll destabilization is in the negative \mathbf{z}_B direction; therefore, the desired inertial loading can be generated by prescribing $\ddot{\xi} > 0$ (section 3.2) during this gait half-cycle, and the desired gravitational loading can be generated by enforcing $\eta_1 > 0$ during this gait half-cycle. Conversely, when legs A and B are in their support and lift phases, respectively, enforce $\ddot{\xi} < 0$ and $\eta_1 < 0$. Based on equations (2) and (3), $\eta_1 > 0$ correlates to $\xi < 0$, and vice versa.

A single biped gait cycle may be defined using three time points: the cycle start at time t_A , in which leg A enters its support phase and leg B enters its lift phase, the cycle's midpoint at time t_C , in which the legs switch phases, and the cycle end at time t_E , which is also the next gait cycle's t_A . By definition, $t_C = (t_A + t_E)/2$. In addition, to aid the model formulation, times $t_B = (t_A + t_C)/2$ and $t_D = (t_C + t_E)/2$ are defined as the midpoints of the first and second gait half-cycles.

To implement the desired $\dot{\eta}$ behavior ($\dot{\eta} > 0$ when leg A is lifted; $\dot{\eta} < 0$ when leg B is lifted), $\dot{\eta}$ is defined by a sinusoidal wave of period $\Delta T = t_E - t_A$ in equation (27), where $\ddot{\xi}_p$ is the peak ξ acceleration. Single- and double-integration of this equation results in formulations for $\dot{\xi}$ (equation (28)) and ξ (equation (29)), where ξ_A and $\dot{\xi}_A$ are the initial roll angle and roll velocity at time t_A . Choices for $\ddot{\xi}_p$, $\dot{\xi}_A$ and ξ_A are dictated by the gravitational loading considerations.

$$\ddot{\xi} = \ddot{\xi}_p \sin\left(2\pi \frac{t - t_A}{\Delta T}\right) \quad (27)$$

$$\dot{\xi} = \dot{\xi}_A + \frac{\Delta T}{2\pi} \ddot{\xi}_p \left(1 - \cos\left(2\pi \frac{t - t_A}{\Delta T}\right)\right) \quad (28)$$

$$\xi = \xi_A + \left(\dot{\xi}_A + \frac{\Delta T}{2\pi} \ddot{\xi}_p\right) t - \left(\frac{\Delta T}{2\pi}\right)^2 \ddot{\xi}_p \sin\left(2\pi \frac{t - t_A}{\Delta T}\right). \quad (29)$$

First, whenever the legs change gait phase, there is a corresponding change in the sign of ξ . To accommodate this, $\xi_A = \xi_C = \xi_E = 0$. In addition to this condition defining ξ_A , evaluating equation (29) at t_C and equating it to $\xi_C = 0$ results in the coupling condition between and defined in equation (30).

$$\dot{\xi}_A = -\frac{\Delta T}{2\pi} \ddot{\xi}_p. \quad (30)$$

With these constraints, ξ has maximum magnitude at times t_B and t_D ; therefore, ξ_B and ξ_D should be scaled such that the tail state $\mathbf{z}_{grv,max}$ (equation (26)) is achievable at this angle. For t_B , at which leg B is lifted, $\xi_B = 90^\circ$ allows for $\eta_1 = -90^\circ$ when $\beta_1 = 90^\circ$. For t_D , at which leg A is lifted, $\xi_D = 90^\circ$ allows for $\eta_1 = 90^\circ$ when $\beta_1 = 90^\circ$. Each of these conditions dictate the equation (31) definition of $\ddot{\xi}_p$.

$$\ddot{\xi}_p = -90^\circ \left(\frac{2\pi}{\Delta T}\right)^2. \quad (31)$$

In addition to the $\xi(t)$ trajectory, a formulation for β is also needed. To isolate the impact of the tail's rolling motion on stability, the angles are fixed as $\beta_1 = 90^\circ$ and $\beta_2 = 0$ to ensure that the tail state matches $\mathbf{z}_{grv,max}$ at t_B and t_D .

7.2. Stabilization case study

For this case study, biped simulations only using simulated tail loading results are generated. Like the maneuvering case study, measurement and modeling uncertainties are considered and the same noise is added into the system to better estimate the real system performance. However, unlike the maneuvering case study, in which the prescribed tail motion was simply a planar bend of the tail, the rolling bending trajectory of the tail is not conducive to the prescribed velocity inner-loop controller that does not incorporate real-time joint position or velocity feedback. As discussed in section 8, work to fully implement the prescribed torque inner-loop controller on the USRT prototype is ongoing.

Figure 12 illustrates the roll-angle trajectories of the biped during a single gait cycle with and without the stabilizing tail action. In the absence of the tail actuation, as the biped begins to lift one of its legs, it begins rolling to the side for which the leg is lifted. As the biped rolls, the leg continues its motion, and at the peak of the roll magnitude, the leg comes in contact with the ground once again, earlier than the anticipated switch between leg contacts at 0.5 s intervals. For the remainder of this gait half-cycle, the foot is in contact with the ground, and is pushing up the biped to its nominal configuration. Alternatively, the controlled biped motion shows a minor roll variation (less than 1°) immediately after the gait transition, but otherwise maintains a stable roll angle throughout the gait cycle.

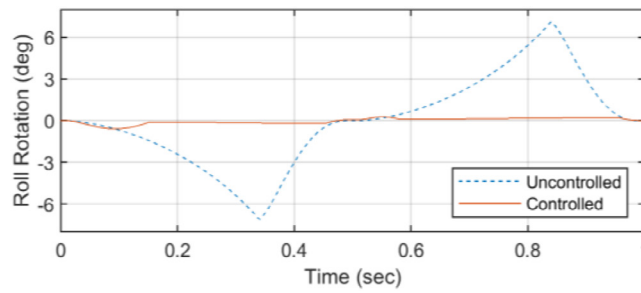


Figure 12. Simulated biped roll angle trajectories with and without stabilizing tail motion. (Generated by ADAMS/MATLAB Co-simulation).

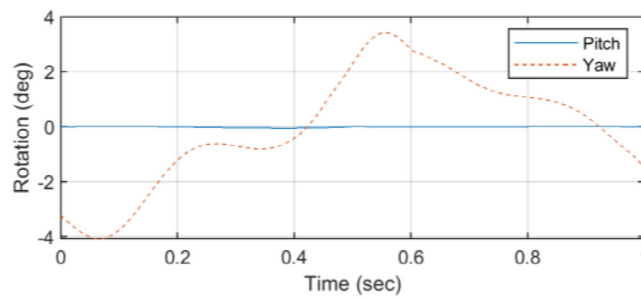


Figure 13. Simulated biped pitch and yaw angle trajectories due to stabilizing tail motion. (Generated by ADAMS/MATLAB Co-simulation).

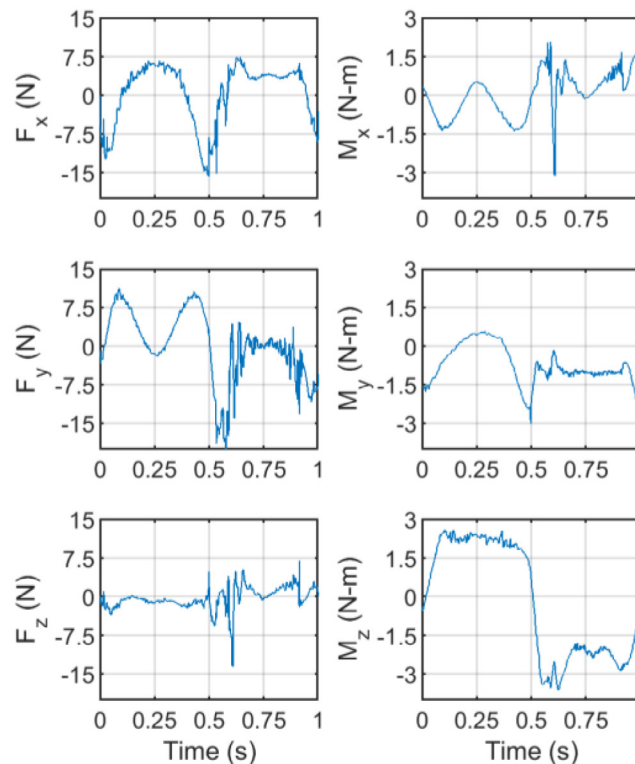


Figure 14. Simulated tail base force and moment loading for stabilizing tail motion. (Generated by ADAMS/MATLAB Co-simulation).

Figure 13 illustrates the ancillary pitch-angle and yaw-angle trajectories of the biped during the stabilizing tail motion. As anticipated, the rolling tail motion causes no apparent change in the bipeds pitch, whereas the bipeds yaw cyclically adjusts due to the cyclic hori-

zontal motion of the tails COM during the stabilizing roll motion. This yaw angle trajectory variation causes no net change in heading angle when averaged over the gait cycle, but slightly reduces the efficiency of locomotion.

The simulated loading profiles are presented in figure 14 to show the behavior of the tails z-component of moment, which correlates to the bipeds roll axis. As desired, the tail generates a consistent stabilizing moment in each half of the gait cycle. Use of an alternative formulation for the tails motion could modify this profile if necessary, but the result is strong considering its source is a sinusoidal waveform.

8. Conclusion

This paper has presented controllers designed to implement maneuvering and stabilization behaviors for a tailed-biped mobile robot. Designs and models for the tail and biped subsystems were presented, along with considerations for sensing along the tail. Prescribed velocity and prescribed torque inner-loop controllers were described, and outer-loop controllers for yaw-angle steering (maneuvering) and roll-angle disturbance rejection while lifting a leg (stabilization) were formulated. Results of case studies for the maneuvering and stabilization outer-loop controllers were presented and demonstrated the two desired functionalities on a simulated bipedal platform.

Although the results in this paper are a promising first step, they motivate a wide range of further research aimed at improving aspects of the integrated tailed-biped system design, modeling and performance. First, in terms of the dynamics of the system, a joint consideration of the biped and tail dynamics in a unified framework is next to allow for better understanding of the coupling effects of these two systems, particularly the impact of the motion of the biped torso on the tail. In terms of performance, this analysis isolated the maneuvering and stabilization behavior; future work will stitch together these functionalities as the biped moves forward. In addition, alternative tail trajectories to implement these and other behaviors, including those that exploit the various mode shapes the two segment tail can provide.

Acknowledgments

This material is based upon work supported by the National Science Foundation under Grant No. 1557312.

ORCID iDs

Yujiong Liu  <https://orcid.org/0000-0003-4926-5109>
Pinhas Ben-Tzvi  <https://orcid.org/0000-0002-9452-482X>

References

- Alexander R M, Maloiy G M O, Njau R and Jayes A S 1979 Mechanics of running of the ostrich (*Struthio camelus*) *J. Zool.* **187** 169–78
- Kingdon J 1971 *East Africa Mammals: an Atlas of Evolution in Africa* vol 1 (London: Academic)
- Aerts P, Aerts P, Van Damme R, D' Août K and Van Hooydonck B 2003 Bipedalism in lizards: whole-body modelling reveals a possible spandrel *Phil. Trans. R. Soc. B* **358** 1525–33
- Benton M J 2010 Studying function and behavior in the fossil record *PLoS Biol.* **8** e1000321
- Persons W S IV and Currie P J 2011 The tail of *Tyrannosaurus*: reassessing the size and locomotive importance of the M. caudofemoralis in non-avian theropods *Anatom. Rec.* **294** 119–31
- Rone W and Ben-Tzvi P 2016 Dynamic modeling and simulation of a yaw-angle quadruped maneuvering with a planar robotic tail *J. Dyn. Syst. Meas. Control* **138** 084502
- Saab W, Rone W S, Kumar A and Ben-Tzvi P 2018 Design and integration of a novel spatial articulated robotic tail *IEEE/ASME Trans. Mechatronics* (accepted)
- Rone W S, Saab W and Ben-Tzvi P 2018 Design, modeling, and integration of a flexible universal spatial robotic tail *J. Mech. Robot.* **10** 041001
- Saab W, Rone W S and Ben-Tzvi P 2017 Robotic modular leg: design, analysis, and experimentation *J. Mech. Robot.* **9** 024501
- Patel A and Braae M 2014 Rapid acceleration and braking: Inspirations from the cheetah's tail *2014 IEEE Int. Conf. on Robotics and Automation (ICRA)* (IEEE) pp 793–9
- Berenguer F J and Monasterio-Huelin F M 2008 Zappa, a quasi-passive biped walking robot with a tail: Modeling, behavior, and kinematic estimation using accelerometers *IEEE Trans. Ind. Electron.* **55** 3281–9
- Chang-Siu E, Libby T, Brown M, Full R J and Tomizuka M 2013 A nonlinear feedback controller for aerial self-righting by a tailed robot *2013 IEEE Int. Conf. on Robotics and Automation (ICRA)* (IEEE) pp 32–9
- Johnson A M, Libby T, Chang-Siu E, Tomizuka M, Full R J and Koditschek D E 2012 Tail assisted dynamic self righting *Adaptive Mobile Robotics* (Singapore: World Scientific) pp 611–20
- Kohut N J, Haldane D W, Zarrouk D and Fearing R S 2012 Effect of inertial tail on yaw rate of 45 gram legged robot *Adaptive Mobile Robotics* pp 157–64
- Patel A and Braae M 2013 Rapid turning at high-speed: inspirations from the cheetah's tail *2013 IEEE/RSJ Int. Conf. on Intelligent Robots and Systems (IROS)* (IEEE) pp 5506–11
- Briggs R, Lee J, Haberland M and Kim S 2012 Tails in biomimetic design: analysis, simulation, and experiment *2012 IEEE/RSJ Int. Conf. on Intelligent Robots and Systems (IROS)* (IEEE) pp 1473–80
- Zhao J, Zhao T, Xi N, Cintrón F J, Mutka M W and Xiao L 2013 Controlling aerial maneuvering of a miniature jumping robot using its tail *2013 IEEE/RSJ Int. Conf. on Intelligent Robots and Systems (IROS)* (IEEE) pp 3802–7
- Mutka A, Orsag M and Kovacic Z 2013 Stabilizing a quadruped robot locomotion using a two degree of freedom tail *2013 21st Mediterranean Conf. on Control & Automation (MED)* (IEEE) pp 1336–42
- Liu G-H, Lin H-Y, Lin H-Y, Chen S-T and Lin P-C 2014 A bio-inspired hopping kangaroo robot with an active tail *J. Bionic Eng.* **11** 541–55
- Saab W, Rone W S and Ben-Tzvi P 2018 Discrete modular serpentine robotic tail: design, analysis and experimentation *Robotica* pp 1–25
- Rone W S and Ben-Tzvi P 2014 Continuum robotic tail loading analysis for mobile robot stabilization and maneuvering *ASME 2014 Int. Design Engineering Technical Conf. and Computers and Information in Engineering Conf.* (ASME) p V05AT08A009
- Saab W, Rone W S and Ben-Tzvi P 2018 Robotic tails: a state-of-the-art review *Robotica* pp 1–15
- Saab W and Ben-Tzvi P 2017 Maneuverability and heading control of a quadruped robot utilizing tail dynamics *ASME 2017 Dynamic Systems and Control Conf.* (ASME) p V002T21A010
- Rone W S 2017 Maneuvering and stabilizing control of a quadrupedal robot using a serpentine robotic tail *2017 IEEE Conf. on Control Technology and Applications (CCTA)* (IEEE) pp 1763–8
- Santiago J L, Gonthina P, Godage I S and Walker I D 2016 Soft robots and kangaroo tails: modulating compliance in

- continuum structures via mechanical layer jamming *Soft Robot.* **3** 54–63
- [26] Godage I S, Branson D T, Guglielmino E, Medrano-Cerda G A and Caldwell D G 2011 Dynamics for biomimetic continuum arms: a modal approach *2011 IEEE Int. Conf. on Robotics and Biomimetics (ROBIO)* pp 104–9 (IEEE)
- [27] Hannan M W and Walker I D 2003 Kinematics and the implementation of an elephant's trunk manipulator and other continuum style robots *J. Robot. Syst.* **20** 45–63
- [28] Li T, Nakajima K and Pfeifer R 2013 Online learning for behavior switching in a soft robotic arm *2013 IEEE Int. Conf. on Robotics and Automation (ICRA)* (IEEE) pp 1296–302
- [29] Braganza D, Dawson D M, Walker I D and Nath N 2007 A neural network controller for continuum robots *IEEE Trans. Robot.* **23** 1270–7
- [30] Chitrakaran V K, Behal A, Dawson D M and Walker I D 2007 Setpoint regulation of continuum robots using a fixed camera *Robotica* **25** 581–6
- [31] Camarillo D B, Carlson C R and Salisbury J K 2009 Configuration tracking for continuum manipulators with coupled tendon drive *IEEE Trans. Robot.* **25** 798–808
- [32] Bajo A, Goldman R E and Simaan N 2011 Configuration and joint feedback for enhanced performance of multi-segment continuum robots *2011 IEEE Int. Conf. on Robotics and Automation (ICRA)* (IEEE) pp 2905–12
- [33] Gravagne I A, Rahn C D and Walker I D 2003 Large deflection dynamics and control for planar continuum robots *IEEE/ASME Trans. Mechatronics* **8** 299–307
- [34] Tsai L W 1999 *Robot Analysis: the Mechanics of Serial and Parallel Manipulators* (New York: Wiley)